This paper is published on:

Journal of Constructional Steel Research, Volume 144, May 2018, P135-152.

Pseudo-static tests of terminal stirrup-confined concrete-filled rectangular steel tubular columns

Fa-xing Ding [a, b], Liang Luo [a,*], Liping Wang [a], Shanshan Cheng [c], Zhi-wu Yu [a, b]

[a] School of Civil Engineering, Central South University, Changsha, China.

[b] Engineering Technology Research Center for Prefabricated Construction Industrialization of Hunan Province, Changsha, China.

[c] School of Engineering, University of Plymouth, United Kingdom.

*Corresponding author, Ph.D., E-mail: luoliang1220@csu.edu.cn

ABSTRACT： This paper mainly presents a pseudo-static test program on 12 terminal stirrup-confined square concrete-filled steel tube (SCFT) columns and 14 rectangular SCFT columns under constant axial pressure. The effects of various factors on the hysteretic behavior of specimens are investigated. These factors include with or without stirrups, height of terminal stirrup region, equivalent stirrup ratio, stirrup form, loading direction, height-length ratio (L/B), length-width ratio (B/D), axial compression ratio (n) and sliding support. The failure mode, strain ratio, hysteretic curve, skeleton curve, ultimate bearing capacity, ductility, stiffness degradation, energy dissipation, as well as the residual deformation of the specimens are analyzed. The results indicate that: (1) When n is relatively larger, the bidirectional stirrups can effectively delay the local buckling of steel tube and greatly increase the ultimate bearing capacity, stiffness, equivalent damping viscosity index, residual deformation rate and ductility index, and further significantly improve the seismic behavior of the rectangular SCFT columns; (2) Axial pressure can improve the confinement effect from the steel tube to the core concrete, also bidirectional stirrups can directly confine the core concrete to decrease strain ratio of the steel tube; (3) With the same value of n, increasing the height of terminal stirrup region or increasing the equivalent stirrup ratio can effectively improve the seismic behavior of the rectangular SCFT columns; (4) The influence of loading direction, L/B and B/D on the ductility of rectangular SCFT columns are not obvious.

Keywords: Rectangular concrete-filled steel tubular column; Terminal stirrup; Pseudo-static test; Seismic behavior; Ultimate bearing capacity; Ductility index

1. Introduction

Concrete filled steel tubular (CFT) columns have been increasingly used in bridges and high-rise buildings due to their enhanced compressive strength and stiffness, improved ductility and higher energy absorption capacity compared to the conventional steel or concrete structures. With such benefits, the use of CFT columns is becoming more commonplace and the performance of CFT columns has caught more and more research attention [1-9]. Several studies have demonstrated that circular CFT stub columns can provide sufficient constraint from the steel tube to the core concrete [1-4]. However, the flexural rigidity and flexural capacity are comparatively low and, in particular, the configuration of joints connecting the circular CFT columns and beams is complex. In comparison, the confining effect from the steel tube to the core concrete in square or rectangular CFT columns is relatively weak, despite that the section moment of inertia (therefore bending stiffness) is improved and the joint configuration is more convenient [5-9]. However, the confining effect from the steel tube to the concrete in rectangular CFT columns is relatively weak and the load-bearing capacity and ductility under seismic action are therefore reduced. The seismic behavior of rectangular CFT members is increasingly becoming a critical problem in the engineering field [10-12].

Pseudo-static tests are usually used to study the seismic performance of CFT columns, that is, axial compression and lateral cyclic load are applied to columns simultaneously. Amit H. Varma et al. [10] conducted a pseudo-static test study on 8 square CFT columns to investigate the effects of parameters include width to thickness ratio, steel yield strength and axial compression ratio n on the seismic behavior of such members. The experimental results show that there is no obvious difference of the displacement ductility index when the steel ratio of cross section is changed from 7.5% to 11.0%. Also, when n is 0.21, the displacement ductility index of conventional steel specimens is not obviously different from high strength steel specimens. Similarly, Liu et al. [11] conducted a seismic behavior test study on 9 square CFT columns with the steel ratio ranged from 6.9% to 12.4% under constant axial load and lateral cyclic load. Effects of n, width to thickness ratio, height-length ratio and concrete strength on the ductility and energy dissipation ability were studied. Han et al. [12] focused on ultimate bearing capacity and ductility on 12 square CFT columns and 18 rectangular CFT columns with the steel ratio during 8.6%~14.5% under a pseudo-static test study. Three key parameters including n, length-width ratio and core concrete strength were considered in the experimental study. The results from the above studies reflected that when n is more than 0.5, the ductility and energy dissipation of the square CFT columns and rectangular CFT columns are generally low.

Moreover, many researchers have proposed different structural measures on square CFT columns in order to increase the confinement effect from the steel tube to the core concrete and improve their seismic performance. These structural measures include steel jacket welded outside the steel tube [13], encased profile steel [14], longitudinal stiffening ribs [15] and horizontal binding bars [16] arranged inside the steel tube. Mao et al. [13] proposed 3 forms of steel jackets welded to the potential plastic hinge region to delay the local buckling of the steel tube and ensure a ductile behavior of CFT members. However, due to the limitation of welding technology, the improvement of ultimate bearing capacity and stiffness is not obvious. The structural measures outside the steel tube are mainly applied to the reinforcement of the existing CFT members. On the other hand, for the new CFT members, increasing the internal steel is usually applied to improve the steel ratio. For example, Zhu et al. [14] proposed profile steel embedded in core concrete to prevent the fracture surface of concrete under failure load. When the equivalent amount of steel is increased by 97.8%, ultimate bearing capacity, displacement ductility index, energy-dissipation index are increased by 9.5%, 15.4%, 13.5%. Zhang et al. [15] proposed longitudinal stiffening ribs on 2 inner faces or 4 inner faces of square steel tubes. It was found that when n is 0.4 and 0.5, compared to the specimen of 2 stiffening ribs, the specimen with 4 stiffening ribs have no obvious improvement in the ultimate bearing

capacity compared to the specimen with 2 stiffening ribs. However, its displacement ductility index is increased by 30%. Wang et al. [16] proposed a measure by bolting horizontal binding bars inside the square steel tubes to postpone their local buckling and improve the seismic behavior of CFT specimens. The results show that when n is 0.2, the ultimate bearing capacity is almost unchanged while the ductility index is increased by 67%. Moreover, when n is 0.6, the ultimate bearing capacity is increased by 10% and the ductility index is increased by 30%.

However, it is difficult to perform the welding work for large-dimensional CFT columns due to their too thick steel tube in practical project. Consequently, the thin-walled rectangular CFT columns have been widely used. However, the latters' low steel ratio will weaken their seismic performance. In order to improve the axial compressive performance of thin-walled square CFT stub columns, Ding *et al*. [17] conducted a comparison study of four structural measures including studs, circular stirrups, rhombus stirrups and bidirectional stirrups, based on which they proposed a way of welding the bidirectional stirrups to the inner wall of the square steel tube. This method was proved to exert the most effective constraint on the core concrete and hence was applied to round-ended CFT stub columns under axial compression [18]. Similarly, it can also be applied to the rectangular CFT columns for the study on seismic performance.

It is known that the weak region of a CFT frame column is located at its terminal section, the idea of stirrups encryption in joint area of reinforced-concrete structure can be applied to CFT columns. In order to reduce the amount of steel, improve the economic efficiency and optimize the construction, the authors put forward the terminal stirrup-confined rectangular CFT (SCFT) columns in which the bidirectional stirrups are welded inside the rectangular steel tube at the columns ends with large bending moment. For large-dimensional CFT columns, it is convenient for operators entering the steel tube and welding stirrups only at the columns ends.

In conventional standards, storey height and storey number are limited in order to limit n of the columns and ensure their seismic performance. However, in actual high-rise and super high-rise buildings, n of columns is often very large, even reaching 0.8. The aim of this study, therefore, is to focus on the advantage of rectangular SCFT columns under high n even up to 0.8. More specifically, two objectives are included in this study: (1) to investigate the seismic behavior of rectangular SCFT columns through a pseudo-static test study on 26 specimens; (2) to study the effects of 9 main factors on the hysteretic behavior of specimens include with or without stirrups, height of terminal stirrup region, equivalent stirrup ratio, loading direction, height-length ratio (L/B), length-width ratio (B/D), axial compression ratio (n) and sliding support.

2. Experimental investigation

2.1 Specimens and materials

In this test program, 26 specimens were designed, including 12 square SCFT columns and 14 rectangular SCFT columns. Each specimen consisted of concrete filled steel tubular column, top plate, bottom plate and stiffening ribs. Fig. 1 and Fig. 2 exhibit a schematic view and the actual photos of the specimens, respectively. The details of the labels and parameters of specimens are listed in Table 1. In the label of specimen, the first letter "s" or "r" represents square or rectangle, the second letter "c" means column, the third letter "h" indicates that the loading mode is hysteretic. B is the length (longer side) of rectangular section, D is the width (shorter side) of the rectangular section, t is the wall thickness of the steel tube, L is the effective height of column excluding the height of stiffening ribs. ρ_s is the steel ratio of the cross section, calculated by $\rho_s=A_s/(A_s+A_c)$, where A_s and A_c are the area of steel tube and core concrete, respectively. a_s, b_s and d_s are horizontal spacing, longitudinal spacing and diameter of stirrups, respectively. h_1 and h_2 are height of terminal stirrup region at the bottom and top of specimens. Stirrups of h_1 mainly bear the bending moment and shear force, while stirrups of h_2 are constructional reinforcement to prevent

the core concrete from premature crushing failure. f_{cu} is the cubic compressive strength of concrete, f_c is uniaxial compressive strength of concrete prism. According to Ding *et al*. [19], the conversion relationship between f_c and concrete compressive strength f_{cu} is f_c=0.4$f_{cu}^{7/6}$. f_s and f_{sv} is the yield strength of steel tube and stirrup, respectively. ρ_{sa} is equivalent stirrup ratio defined as $\rho_{sa}=\rho_{sv}\times f_{sv}/f_s$, where ρ_{sv} is the stirrup ratio. n is axial compression ratio, calculated by $n= N/N_u$, where N is the constant axial pressure and N_u is the nominal bearing capacity. N_u is obtained from formula $N_u=f_cA_c+f_yA_s$ [11, 15, 16]. P^+ and P^- are the maximum positive and negative horizontal bearing capacity. DI is the displacement ductility index obtained from the average value of positive and negative displacement ductility index. K_1 is the initial stiffness obtained from the average value of positive and negative initial stiffness.

Among these specimens, sch1 and sch3 are without stirrups while the others are with bidirectional stirrups on the cross-sections of specified spacing. Besides, sch1, sch2 and sch5 were tested without sliding support because the n of sch1, sch2 is 0 and sch5 is used to compare the effect of sliding support with sch3. Moreover, the stirrup diameter of sch8 is 8 mm and sch9 is with ring stirrups. Particularly, the n of rch1~4-0.8 is up to 0.8.

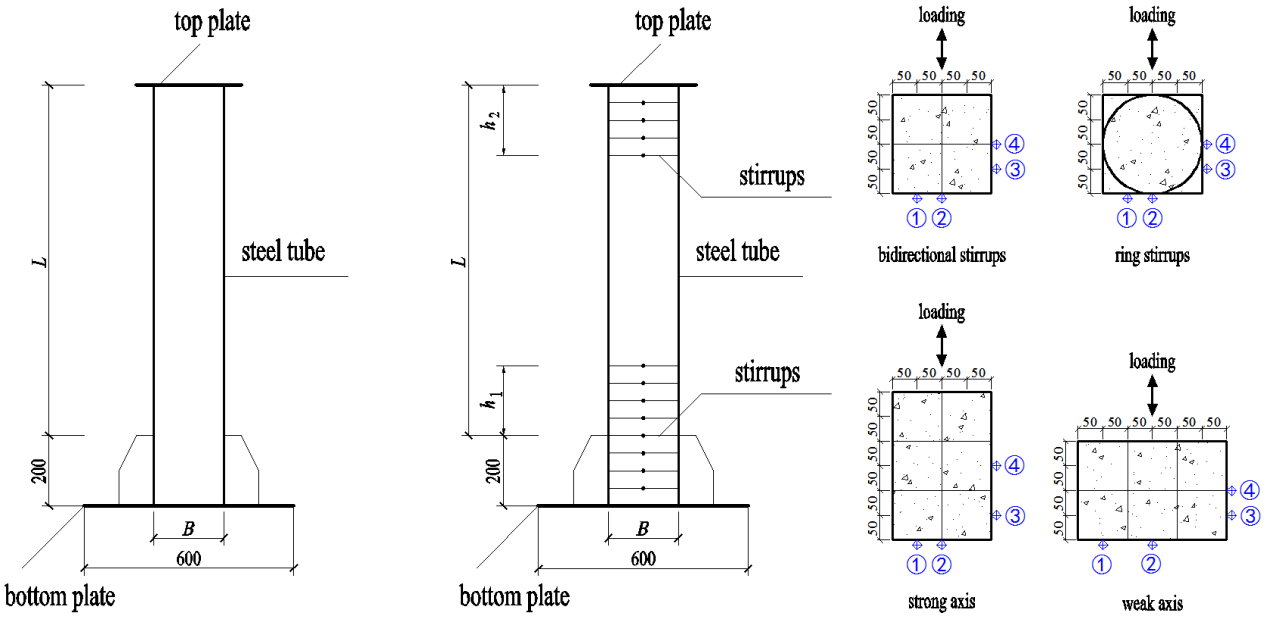

(a) Specimens without stirrups (b) Specimens with stirrups (c) Sectional forms and strain rosettes arrangement

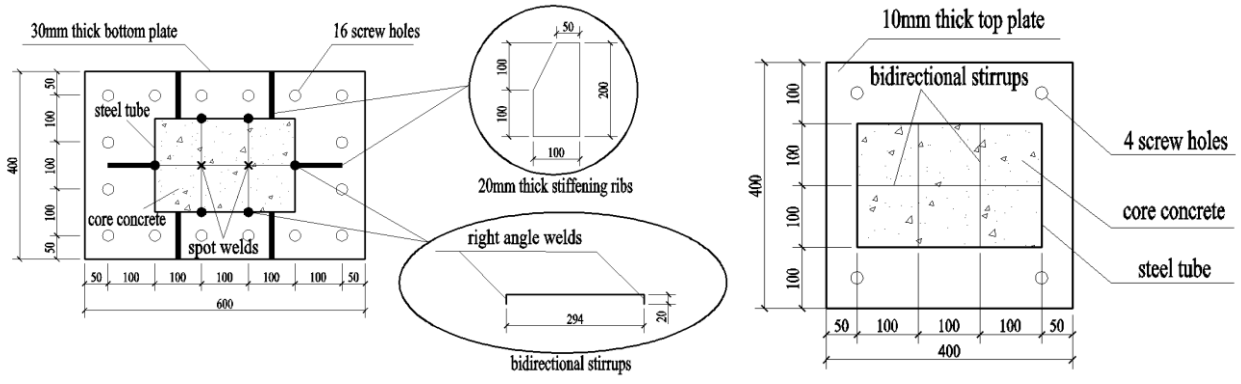

(d) Bottom plate, stiffening ribs and stirrup welding (e) Top plate

Fig.1. schematic view of specimens

(a) Top plate and sliding support (b) Bottom plate and stiffening ribs (c) Stirrup welding

Fig.2. Actual diagram of specimens

Table 1 Parameters of specimens

(a) Square SCFT columns

Specimen	$B\times D\times t\times L$/mm	ρ_s	a_s/mm	b_s/mm	d_s/mm	h_1	h_2	f_{cu}/MPa	f_c/MPa	f_s/MPa	f_{sv}/MPa	ρ_{sa}	n	N/kN	sliding support	P^+/kN	P^-/kN	DI	K_1/(kN/mm)
sch1	200×200×3×1500	0.06	-	-	-	0	0	43.2	32.4	368	285	-	0	0	without	54.62	53.96	5.02	3.50
sch2	200×200×3×1500	0.06	100	50	6	200	200	43.2	32.4	368	285	0.45%	0	0	without	56.36	57.27	6.12	3.75
sch3	200×200×3×1500	0.06	-	-	-	0	0	43.2	32.4	368	285	-	0.4	835.7	with	61.02	58.54	3.74	4.11
sch4	200×200×3×1500	0.06	100	50	6	200	200	43.2	32.4	368	285	0.45%	0.4	835.7	with	70.15	68.48	4.38	4.27
sch5	200×200×3×1500	0.06	100	50	6	0	0	43.2	32.4	368	285	0.45%	0.4	835.7	without	66.28	66.81	3.35	3.87
sch6	200×200×3×900	0.06	100	50	6	200	200	43.2	32.4	368	285	0.45%	0.4	835.7	with	95.71	96.88	4.71	17.63
sch7	200×200×3×1500	0.06	100	50	6	400	200	43.2	32.4	368	285	0.45%	0.6	1253.6	with	52.03	50.34	2.85	5.08
sch8	200×200×3×1500	0.06	100	50	8	400	200	43.2	32.4	368	504	1.42%	0.6	1253.6	with	83.54	79.39	3.02	5.76
sch9	200×200×3×1500	0.06	ring	50	6	400	200	43.2	32.4	368	285	0.73%	0.6	1253.6	with	48.40	47.23	2.38	4.68
sch10	200×200×3×2000	0.06	100	50	6	200	200	43.2	32.4	368	285	0.45%	0.2	417.9	with	47.58	45.29	4.62	1.92
sch11	200×200×3×2000	0.06	100	50	6	200	200	43.2	32.4	368	285	0.45%	0.4	835.7	with	49.70	49.28	4.08	2.12
sch12	200×200×3×2000	0.06	100	50	6	400	200	43.2	32.4	368	285	0.45%	0.6	1253.6	with	47.81	48.51	2.63	2.43

(b) Rectangular SCFT columns

Specimen	$B\times D\times t\times L$/mm	ρ_s	a_s/mm	b_s/mm	d_s/mm	h_1	h_2	f_{cu}/MPa	f_c/MPa	f_s/MPa	f_{sv}/MPa	ρ_{sa}	n	N/kN	sliding support	P^+/kN	P^-/kN	DI	K_1/kN/mm
rch1	300×200×3×1500	0.05	100	50	6	300	200	43.2	32.4	368	285	0.52%	0.2	587.7	with	147.78	157.65	4.54	8.34
rch2	300×200×3×1500	0.05	100	50	6	300	200	43.2	32.4	368	285	0.52%	0.4	1175.5	with	134.96	135.94	4.27	9.85
rch3	300×200×3×1500	0.05	100	50	6	300	200	43.2	32.4	368	285	0.52%	0.7	2057.1	with	117.59	126.28	2.26	12.41
rch4	300×200×3×1500	0.05	100	50	6	600	200	43.2	32.4	368	285	0.52%	0.7	2057.1	with	128.90	133.90	2.67	13.52
rch5	200×300×3×1500	0.05	100	50	6	300	200	43.2	32.4	368	285	0.52%	0.2	587.7	with	110.56	113.16	4.83	5.52
rch6	200×300×3×1500	0.05	100	50	6	300	200	43.2	32.4	368	285	0.52%	0.7	2057.1	with	84.75	86.96	2.48	6.77
rch7	200×300×3×1000	0.05	100	50	6	300	200	43.2	32.4	368	285	0.52%	0.7	2057.1	with	165.23	162.11	2.75	14.28
rch8	300×200×3×2000	0.05	100	50	6	300	200	43.2	32.4	368	285	0.52%	0.2	587.7	with	117.00	117.69	4.12	6.27
rch9	300×200×3×2000	0.05	100	50	6	300	200	43.2	32.4	368	285	0.52%	0.4	1175.5	with	107.89	104.54	3.85	6.82
rch10	300×200×3×2000	0.05	100	50	6	600	200	43.2	32.4	368	285	0.52%	0.6	1763.2	with	105.61	106.34	2.47	5.71
rch1-0.8	300×200×3×1000	0.05	100	-	-	-	-	43.5	32.6	355	-	-		2329.2	with	268.47	226.81	2.07	23.37
rch2-0.8	300×200×3×1000	0.05	100	50	8	600	200	43.5	32.6	355	444	1.49%	0.8	2329.2	with	328.69	316.57	3.71	41.70
rch3-0.8	300×200×3×1000	0.05	100	50	10	300	200	43.5	32.6	355	532	2.79%	0.8	2329.2	with	338.66	343.17	3.70	39.79
rch4-0.8	300×200×3×1000	0.05	100	50	10	600	200	43.5	32.6	355	532	2.79%	0.8	2329.2	with	377.69	364.96	4.17	43.98

For each specimen, the steel tube was welded from two right angle tubes which were firstly bent using the Q235 hot-rolled steel plates. The welding was performed according to the standard GB 50017-2003 [20] and the ends of the steel grooves (as the sites of welding) were kept smooth after welding. Both ends of

stirrups were firstly bent to right angle with bent length of 20 mm and then welded to the two ends of the steel tubes in a certain range. Moreover, spot welds were adopted at the intersections of bidirectional stirrups and thus they form a steel mesh.

The bottom plate and stiffening ribs were welded to the bottom of the steel tube. Then the concrete was pumped into the tube from the top and was vibrated to be well compacted. The commercial concrete of grade C40 was adopted for all the specimens. Moreover, 9 standard concrete cubes with a dimension of 150 mm × 150 mm × 150 mm were prepared and cured at the same condition as those of SCFT specimens. After 28 days of curing, the concrete had hardened completely and achieved its compressive strength. Then the cover plate was welded to the top of the steel tube. For the convenience of observation and record of failure mode, red paint was sprayed on the external surface of the steel tube and 50 mm × 50 mm white grids were plotted on the surface.

Before the column tests, the cubic compressive strength f_{cu} of concrete were obtained from the testing of the concrete cubes according to GB/T 50081-2002 [21]. The material properties of 3 mm thick steel plates and stirrups of diameter 6mm and 8 mm were obtained from the tensile coupon tests according to GB/T 228-2002 [22]. The measured material properties are presented in Table 1.

2.2 Experimental setup and instrumentation

The pseudo-static tests on rectangular SCFT column specimens were conducted using a MTS pseudo-static test system in the National Engineering Laboratory for Construction Technology of High Speed Railway at Central South University. Fig. 3 and Fig. 4 present the schematic diagram and the actual photos of the tests. A top plate was fixed with the sliding support by bolts and to transmit the vertical axial pressure. Besides, a bottom plate was fixed with a custom-made reinforced concrete base by bolts. Then the base was fixed with rigid floor through anchor bolts. The base was strictly reinforced and debugged to eliminate any possible failure during testing. The vertical load was exerted to the specimens through a 2500 kN hydraulic jack tensioned by rebars. The oil pump was manually controlling to ensure the vertical load be stable. The horizontal low cyclic load was exerted by the MTS system hydraulic actuator through the loading chunk.

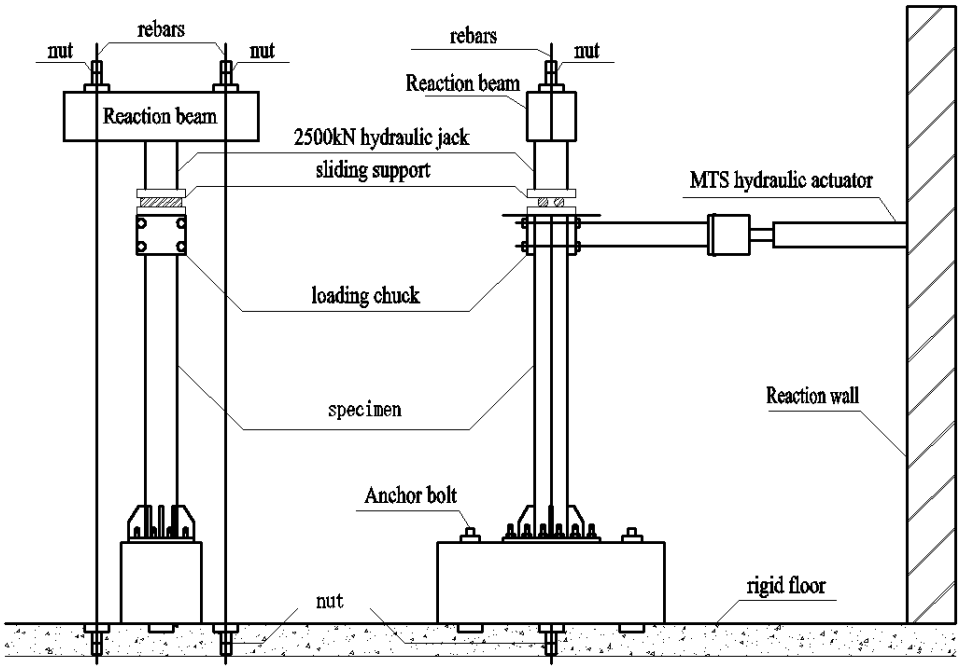

(a) Front view **(b) Side view**

Fig.3. Schematic diagram of test

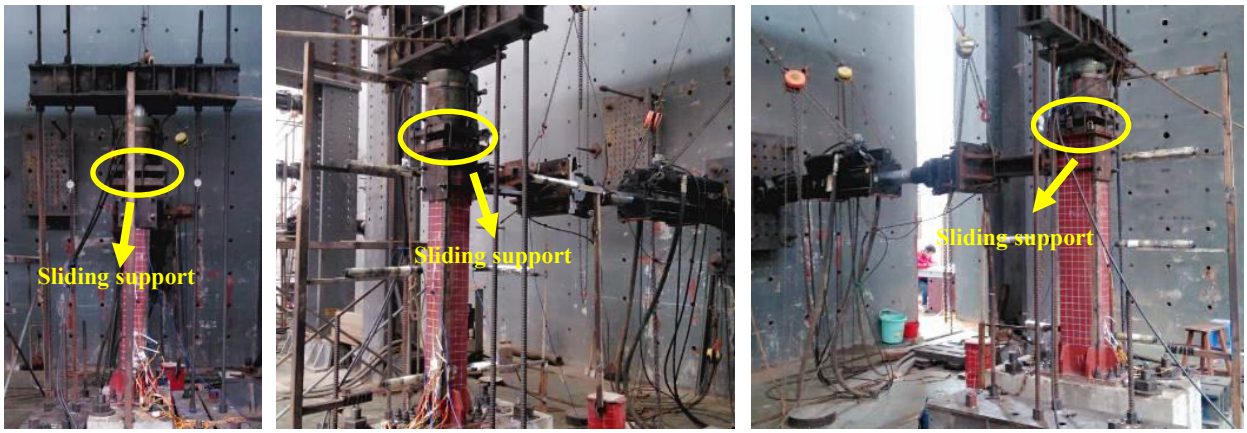

(a) Front view of sch8 **(b) Side view of sch8** **(c) Side view of rch1**

(d) Front view of rch7 **(e) Side view of rch1-0.8** **(f) Front view of rch1-0.8**

Fig.4. Actual diagram of test

At the beginning of each test, the specimen was prepressed to a vertical load to 50% of the specified axial pressure *N*, then unloaded to 0, after that the specimen was loaded to *N* before the lateral force was applied. The axial pressure *N* was kept constant during the whole test. According to JG101-1996 [23], the displacement controlled method was use for horizontal cyclic loading shown in Fig.5. One loading cycle was applied for each of the peak displacement, (1, 1.5, 2, 3, 4, 5~16)Δ_y. Here Δ_y is experimental yield displacement. Such a loading procedure was attempted until the horizontal load of the specimen decreased to 85% of the horizontal bearing capacity.

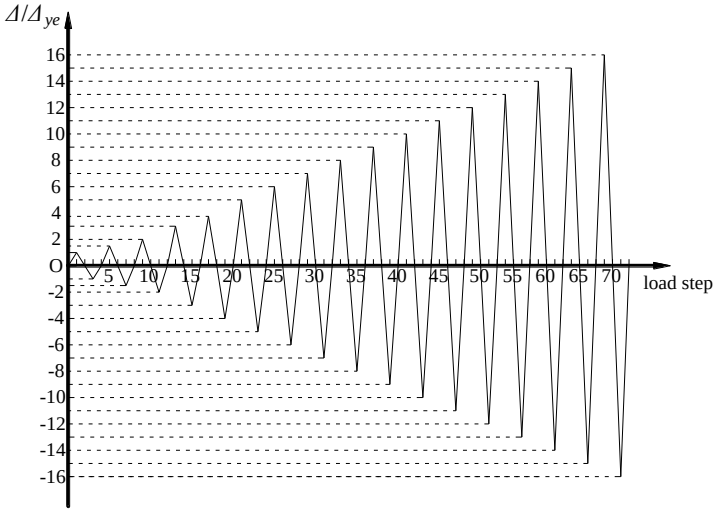

Fig.5. Displacement loading system

2.3 Measuring point arrangement

The horizontal load, horizontal displacement and strain of steel tube were measured during the tests. The horizontal load was collected by the MTS actuator and recorded manually by the tester. Three displacement transducers with high precision were installed at three deferent places, namely at the same height as the horizontal loading point, half of the column height and the bottom of the specimens, respectively, to measure horizontal displacement. Moreover, four strain rosettes (S1 to S4) were placed on two adjacent surfaces at the bottom of the steel tube, as illustrated in Fig. 1 (c). The displacement and strain were acquired by a DH3818 static data measurement system. The local buckling deformation of steel tube, failure mode and failure location during the tests were also observed and recorded.

3. Experimental results and discussion

3.1 Damage mechanism

The damage process of the specimens was basically the same, which could be divided into 3 stages including elastic stage, elastic-plastic stage and failure stage. At the elastic stage of loading, the load-displacement curve of each specimen was basically linear. There was no obvious local buckling on the surface of the steel tube, and the strain was small. As the horizontal displacement increased, the specimens turned into elastic-plastic stage. The stiffness of them degraded and the load increased slowly. The steel tube displayed apparent local buckling above the stiffening ribs. As the test progressed, the range and degree of the local buckling was increasing continuously. When the horizontal load dropped below 85% of the ultimate bearing capacity, the specimens were failed. At this stage, the strain of steel tube increased rapidly with severe buckling (together with tearing at the corner of sections in some cases) in the region of stirrups and extended region of 50 mm above the stirrups. Moreover, the internal stirrups were snapped with crisp sound which indicated that the strain of stirrups reached the ultimate strain and their tensile strength was fully utilized. The final failure modes of the typical specimens are shown in Fig. 6.

Especially when n was up to 0.8, rch1-0.8 (without stirrups) showed obvious axial compression, the steel tube was torn with a large area along the weld, the stirrups were snapped and the core concrete was completely crushed, which is characterized by brittle failure. Unlike this, the steel tube of rch2-0.8 (ρ_{sa}=1.49%) displayed apparent local buckling at the bottom. Even better, only slight local buckling occurred at the bottom of rch3-0.8 (ρ_{sa}=1.49%) and rch4-0.8 (ρ_{sa}=1.49%). Besides, the core concrete of rch2-0.8, rch3-0.8 and rch4-0.8 was only partially crushed, which is characterized by ductile failure. These indicate that the stirrups can effectively pull the steel pipe and confine the core concrete.

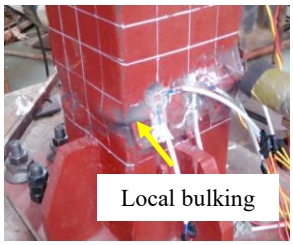

(a) sch1

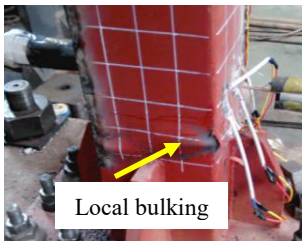

(b) sch2

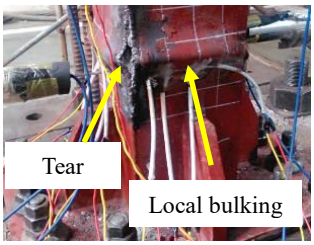

(c) sch3

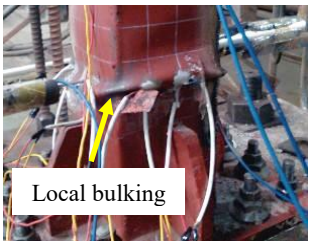

(d) sch4

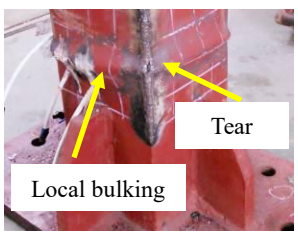

(e) sch6

(f) sch8

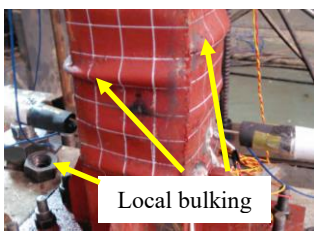

(g) sch12

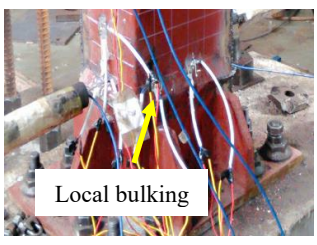

(h) rch1

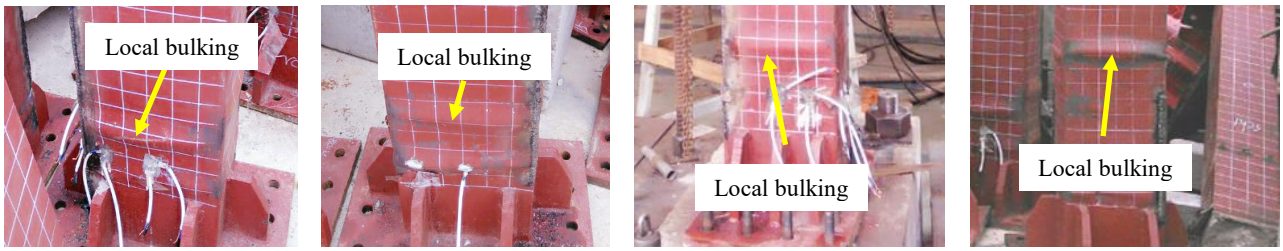

(i) rch3 (j) rch4 (k) rch6 (l) rch10

(m) Steel tube of rch1~4-0.8 (n) Core concrete of rch1~4-0.8

Fig.6. Typical failure modes of specimens

3.2 Load-strain ratio (P-v_{sc}) curves

Fig. 7 presents the load-strain ratio (P-v_{sc}) curves of 5 typical specimens including sch1, sch3, sch4, rch1-0.8 and rch2-0.8. As shown in Eq. (1), the v_{sc} is defined as the absolute value of ratio of circumferential strain to axial strain of the steel tube, reflecting the hoop constraint of the steel tube exerting on the core concrete [17, 24]. The larger the v_{sc} is, the stronger the hoop constraint is.

$$v_{sc} = \frac{\varepsilon_p}{\varepsilon_a} \tag{1}$$

As the horizontal cyclic displacement is applied, the axial strain and circumferential strain of the steel tube varies continuously, which make the strain ratio v_{sc} oscillates. Besides, the maximum v_{sc} of the 5 specimens exceeded 0.5 in the tests. The results suggest that the steel tube of all the 5 specimens exerted the hoop constraint on the core concrete. The maximum v_{sc} of 3.0 for sch3 (with n=0.4) is greater than that of 2.0 for the sch1 (without axial pressure). It is demonstrated that the axial pressure can increase the confining effect of the steel tube exerting on the core concrete. The maximum v_{sc} of 1.5 for sch4 (with stirrups) is less than that of 3.0 for sch3 specimen (without stirrups). Similarly, the maximum v_{sc} of 3.5 for rch2-0.8 (with stirrups) is less than that of 4.5 for rch1-0.8 (without stirrups). This indicates that the maximum v_{sc} of the steel tube is reduced due to the direct confining effect of the stirrups exerting on the core concrete.

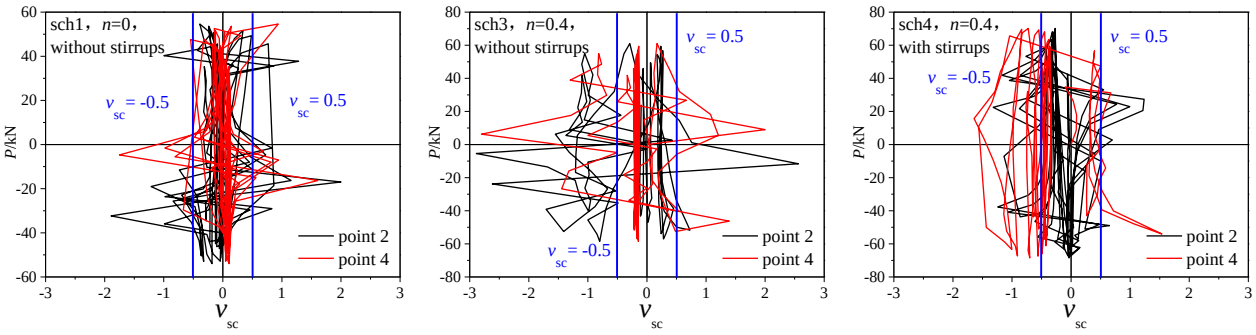

(a) sch1 (n=0, without stirrups) (b) sch3 (n=0.4, without stirrups) (c) sch4 (n=0.4, with stirrups)

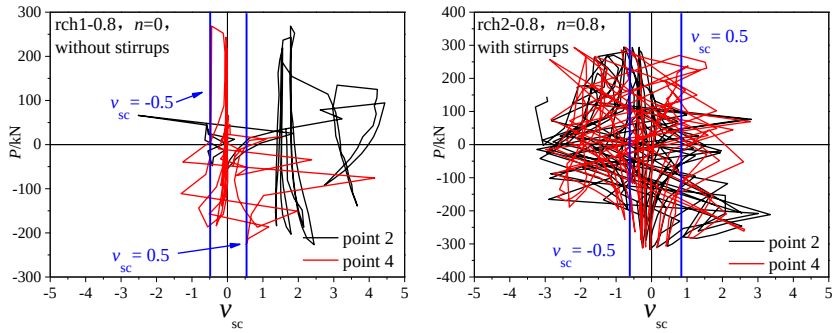

(d) rch1-0.8 (n=0.8, without stirrups) (e) rch2-0.8 (n=0.8, with stirrups)

Fig.7. P-v_{sc} curve of 5 typical specimens

4. Effects of parameters on seismic behavior

4.1 Seismic behavior indexes

In this paper, 5 seismic behavior indexes are analyzed including horizontal bearing capacity P, ductility, stiffness degradation, energy-dissipation capacity and residual deformation. The horizontal bearing capacity is obtained directly from experimental results. The ductility of the specimens is expressed by the displacement ductility index DI, which is defined as the ratio of the failure displacement Δ_u over the virtual yield displacement Δ_{yv} as shown in Eq. (2):

$$DI = \frac{\Delta_u}{\Delta_{yv}} \tag{2}$$

The displacement ductility index is determined by the "General yield bending moment method" (also known as "tangent method") [25], as shown in Fig. 8. OC is the tangent of the P-Δ skeleton curve ($ODFAB$) at origin point O, P_{yv} and Δ_{yv} are the virtual yield load and the corresponding displacement, P_{max} and Δ_{max} are the ultimate load and the corresponding displacement, P_u is the horizontal failure load equal to 85% of the ultimate load in the descending range of the skeleton curve, Δ_u is the corresponding displacement. According to Eq. (2) and Fig. 8, the displacement ductility indices DI of all specimens are listed in Table 1.

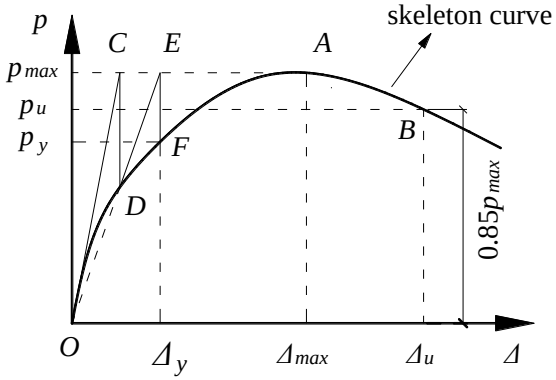

Fig.8. Ductility index obtained from general yield bending moment method

The annular stiffness K [13, 15] is used to evaluate the stiffness degradation of the specimens, which is obtained from Eq. (3):

$$K = \frac{\sum_{i=1}^{n} P^i}{\sum_{i=1}^{n} \Delta^i} \tag{3}$$

where P^i and Δ^i are respectively the peak horizontal load and the corresponding displacement of the i-th cycle, n is the total number of hysteresis loops.

The equivalent viscous damping index h_e [15, 26] is used to estimate the energy-dissipation capacity

of the specimens, defined as Eq. (4):

$$h_e = \frac{1}{2\pi}\frac{S_{ABCDA}}{S_{(OBE+ODF)}} \tag{4}$$

where S_{ABCDA} is the area of each hysteresis loop $ABCD$ (the purple area), $S_{(OBE+ODF)}$ are the total area of triangle OBE and triangle ODF(the shadow area), indicated in Fig.9.

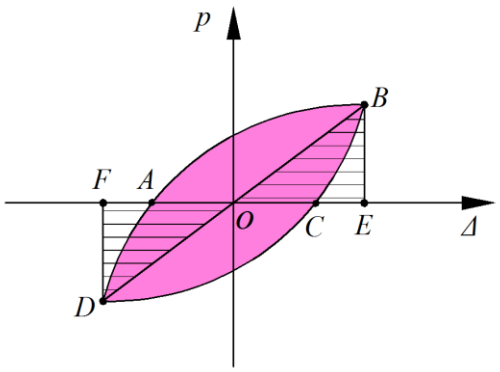

Fig.9. Calculation of equivalent viscous damping index

Residual deformation rate r [27] is defined by Eq. (5):

$$r = \frac{OC^i}{OE^i} \tag{5}$$

where OE^i and OC^i are the maximum displacement and the corresponding residual displacement of the i-th cycle, also indicated in Fig.9.

4.2. Effect of stirrups

Fig. 10 compares the effect of stirrups on the hysteresis behavior when n is 0, 0.4, 0.8 and the ρ_{sa} is 0.45%, 0.45%, 1.49%. Table 2 lists the improvement effect of stirrups on the 5 seismic behavior indexes of the specimens. When n is 0, compared to sch1 without stirrups, the hysteresis curve of sch2 is not obviously different and its P, K_1, maximum h_e, maximum r are only slightly improved. However, the skeleton curve of sch2 declines more slowly and the DI increased by 21.9%. When n is 0.4, compared to sch3 without stirrups, the hysteresis curve of sch4 is plumper and the skeleton curve declines more slowly. In addition, the P, K_1, maximum h_e, maximum r are improved significantly. When n is 0.8, compared to rch1-0.8 without stirrups, all the 5 seismic behavior indexes of rch2-0.8 are improved significantly. It shows more obvious effect of stirrups on improving the hysteresis behavior of rectangular CFT columns under high axial compression ratio.

Index	n=0	n=0.4	n=0.8
Hysteretic curve	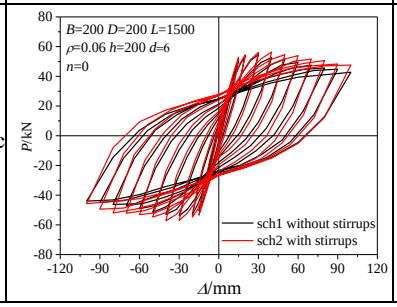	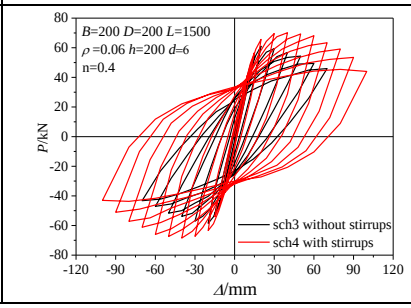	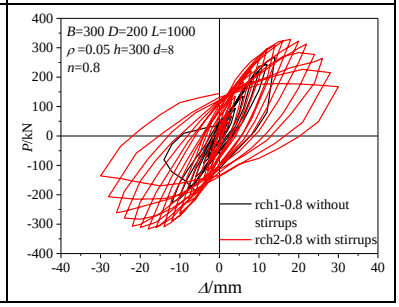

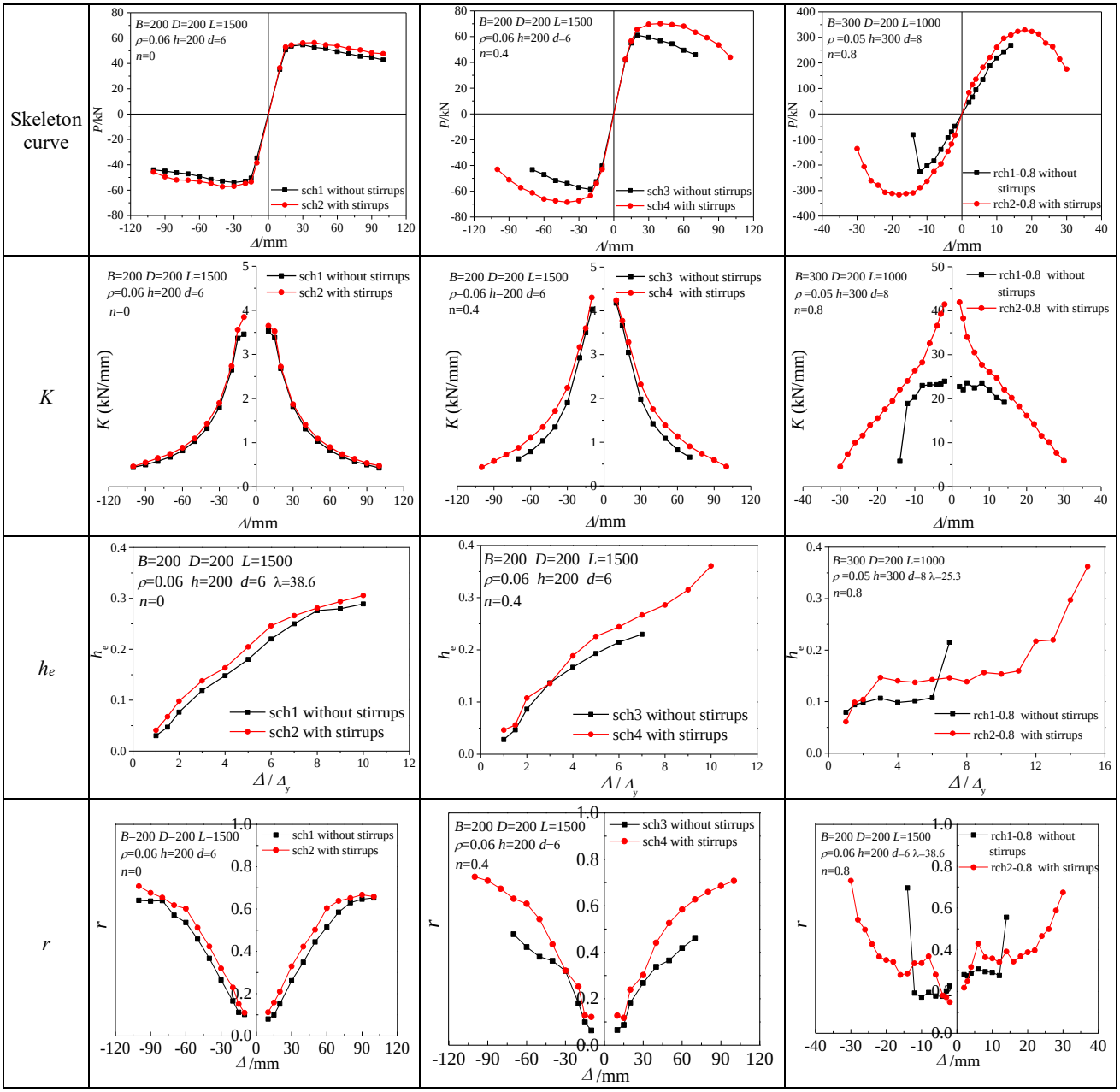

Fig.10. Influence of stirrups on hysteresis behavior when *n* is 0, 0.4 and 0.8

Table 2 Improved effects of stirrups on seismic behavior indexes when *n* is 0, 0.4 and 0.8

Indexes	*n*=0			*n*=0.4			*n*=0.8		
	sch1	sch2	Improve percentage	sch3	sch4	Improve percentage	rch1-0.8	rch2-0.8	Improve percentage
max (P^+, P^-)	54.62	57.27	4.9%	61.02	70.15	15.0%	268.47	328.69	22.4%
DI	5.02	6.12	21.9%	3.74	4.38	17.1%	2.07	3.71	79.2%
K_1	3.5	3.75	7.1%	4.11	4.27	3.9%	23.37	41.70	78.4%
max(h_e)	0.29	0.31	6.9%	0.23	0.36	56.5%	0.22	0.36	63.6%
max(*r*)	0.65	0.71	9.2%	0.48	0.73	52.1%	0.56	0.73	30.4%

4.3. Effect of height of terminal stirrup region

Fig.s 11 and 12 compare the effect of height of terminal stirrup region h_1 on the hysteresis behavior when n is 0.7, 0.8 and the ρ_{sa} is 0.52%, 2.79%. It is reflected from Fig.s 11, 12 and Table 1 that the hysteresis loop is plumper and the skeleton curve tends to decline more slowly when the h_1 is increased from B (300mm) to $2B$ (600mm). Compared to specimen rch3, the P, DI, K_1 of rch4 are increased from 126.28 kN, 2.26, 12.5 kN/mm to 133.90 kN, 2.67, 13.5 kN/mm. On the whole, the 3 indexes are improved

by 6.0%, 18.1%, 8.0% respectively. Besides, stiffness degrades more gently. Furthermore, h_e and r are generally increased at the same loading displacement, which indicates that increasing h_1 can effectively improve the seismic behavior of specimens. Similarly, compared to specimen rch3-0.8, the P, DI, K_1 of rch4-0.8 are improved by 10.1%, 12.4%, 10.5%, respectively.

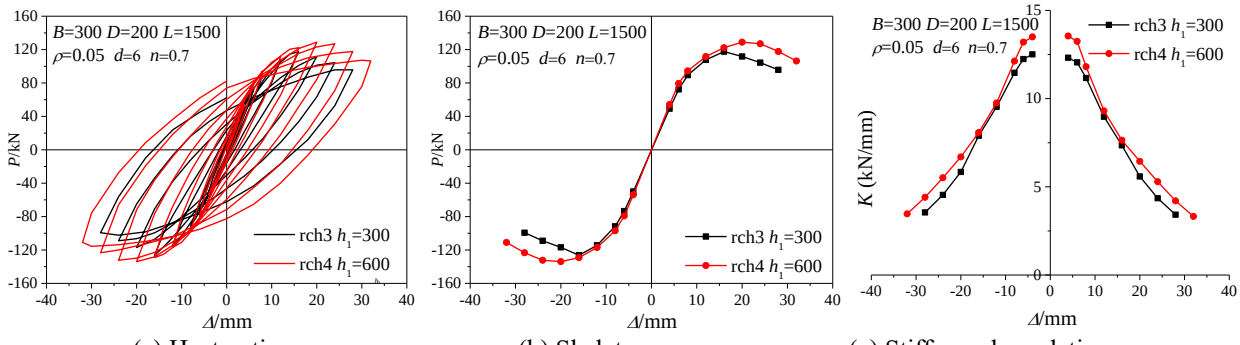

(a) Hysteretic curve (b) Skeleton curve (c) Stiffness degradation

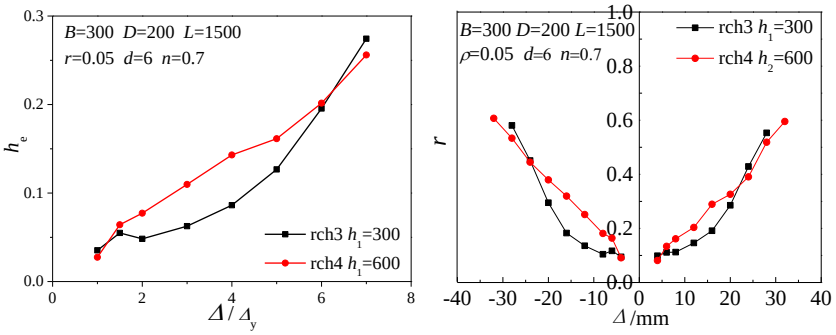

(d) Energy dissipation (e) Residual deformation

Fig.11. Influence of height of terminal stirrup region on hysteresis behavior when *n* is 0.7

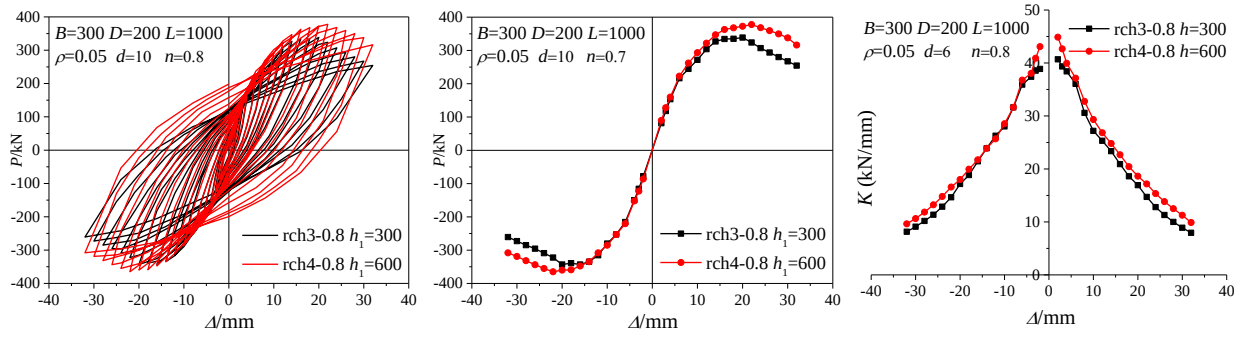

(a) Hysteretic curve (b) Skeleton curve (c) Stiffness degradation

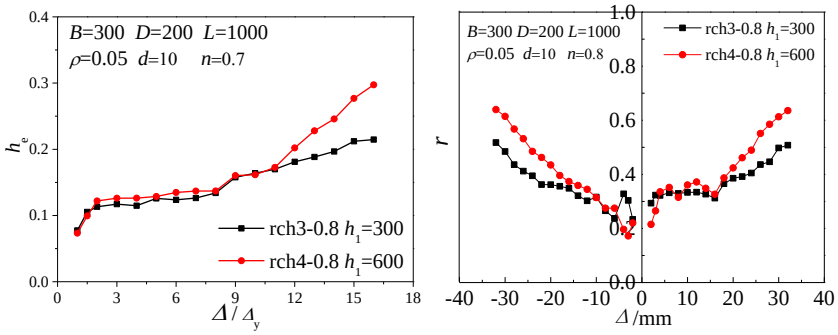

(d) Energy dissipation (e) Residual deformation

Fig.12. Influence of height of terminal stirrup region on hysteresis behavior when *n* is 0.8

4.4. Effect of equivalent stirrup ratio

Fig. 13 compares the effect of equivalent stirrup ratio ρ_{sa} on the hysteresis behavior when n is 0.6 and the stirrups range is 400mm (2B). The diameter d_s of the stirrups are 6mm and 8mm, and the yield strength f_s of the stirrups are 285MPa and 504MPa, respectively. Thus the ρ_{sa} increases from 0.45% to 1.42% and

increased by 215.6%. It can be seen from Fig. 13 and Table 1 that the hysteresis loop is plumper and the skeleton curve declines more slowly when the ρ_{sa} is increased. Compared to sch7, the P, DI, K_1 of sch8 are increased from 52.03 kN, 2.85, 5.12 kN/mm to 83.54 kN, 3.02, 5.87 kN/mm. On the whole, the 3 indexes are improved by 60.6%, 10.2%, 8.0% respectively. In addition, stiffness degrades more gently. At the early stage of loading, the difference of h_e between sch7 and sch8 is not obvious. But at the late stage of loading, the h_e of sch8 was significantly less than h_e of sch7. This is because the horizontal load of sch8 declines slower than that of sch7, and the $S_{(OBE+ODF)}$ in the formula (4) is still larger, resulting in a smaller h_e. However, there is little difference between the r of the 2 specimens. The above analysis contributes that increasing ρ_{sa} can effectively improve the seismic behavior of the specimen.

Similarly, Fig. 14 compares the effect of ρ_{sa} on the hysteresis behavior when n is 0.8 and the stirrups range is 600mm ($2B$). The diameter d_s of the stirrups are 8mm and 10mm, and the yield strength f_s of the stirrups are 444MPa and 532MPa, respectively. Thus the ρ_{sa} increases from 1.49% to 2.79% and increased by 87.2%. Compared to specimen rch2-0.8, the P, DI, K_1 of rch4-0.8 are improved by 14.9%, 12.4%, 5.5%, respectively.

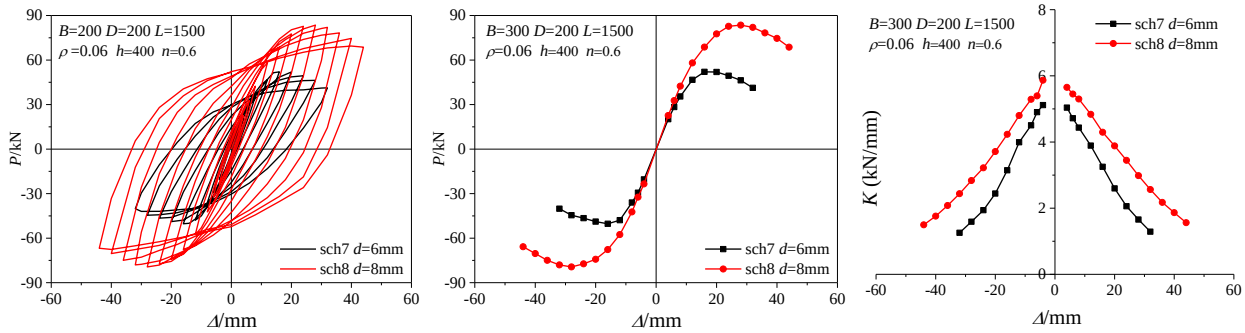

(a) Hysteretic curve (b) Skeleton curve (c) Stiffness degradation

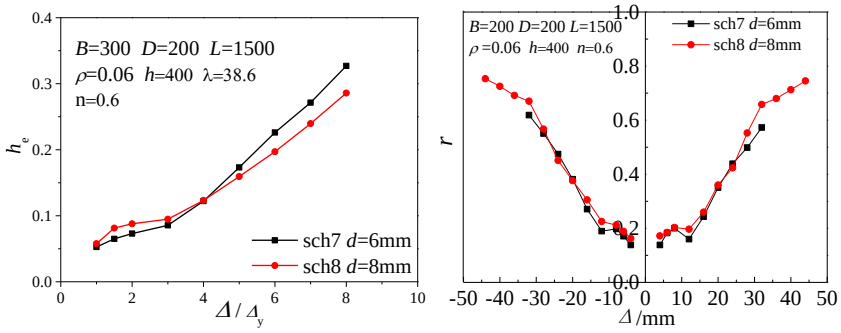

(d) Energy dissipation (e) Residual deformation

Fig.13. Influence of equivalent stirrup ratio on hysteresis behavior when *n* is 0.6

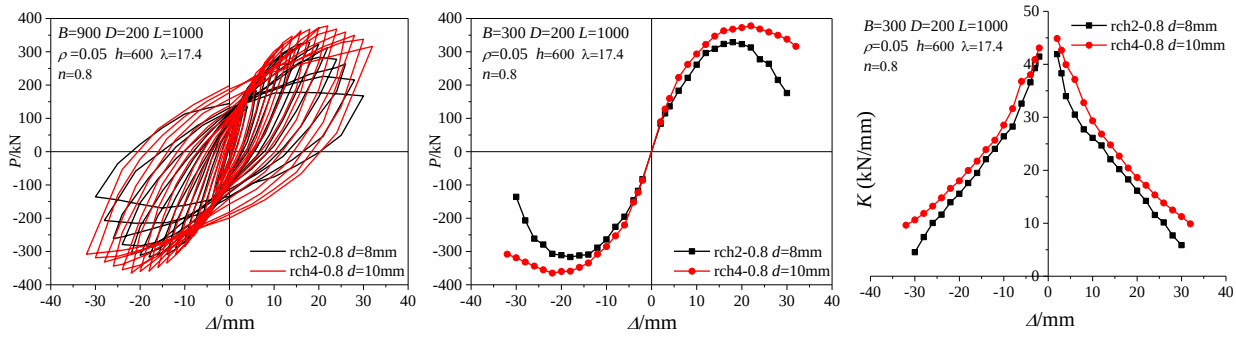

(a) Hysteretic curve (b) Skeleton curve (c) Stiffness degradation

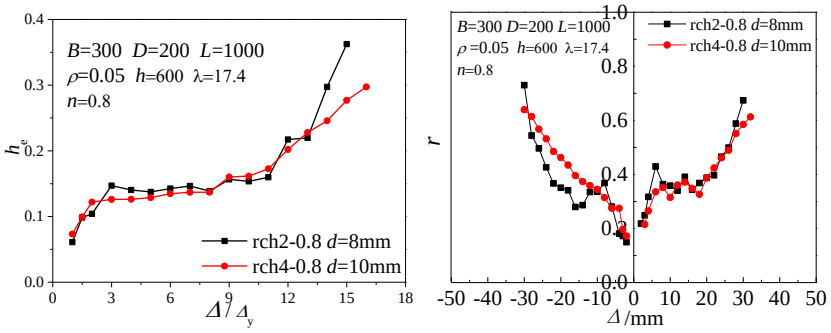

(d) Energy dissipation (e) Residual deformation

Fig.14. Influence of equivalent stirrup ratio on hysteresis behavior when *n* is 0.8

4.5. Effect of stirrup forms

Fig. 15 compares the effect of stirrup forms on the hysteresis behavior when n is 0.6 and the stirrups range is 400mm ($2B$). The ρ_{sa} of sch9 (ring stirrups) and sch7 (bidirectional stirrups) are 0.73% and 0.45% respectively, reduced by 38.4%. However, compared to sch9, the hysteresis loop of sch7 is plumper and its skeleton curve tends to decline more slowly. In addition, The P, DI, K_1 of sch7 are increased from 48.40 kN, 2.38, 4.8 kN/mm to 52.03 kN, 2.85, 5.1 kN/mm. On the whole, the 3 indexes are improved by 7.5%, 19.7%, 6.3%, respectively. Furthermore, h_e and r of sch7 are greater than those of sch9, which state that the seismic behavior of specimen with bidirectional stirrups is superior to specimen with ring stirrups.

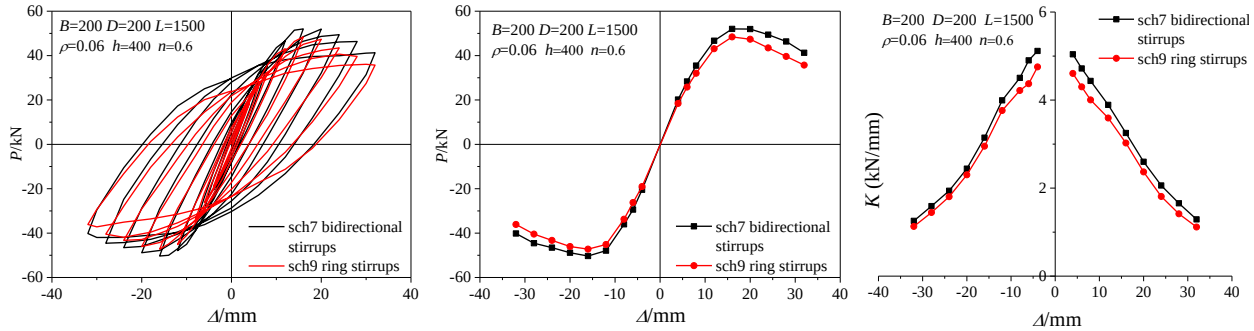

(a) Hysteretic curve (b) Skeleton curve (c) Stiffness degradation

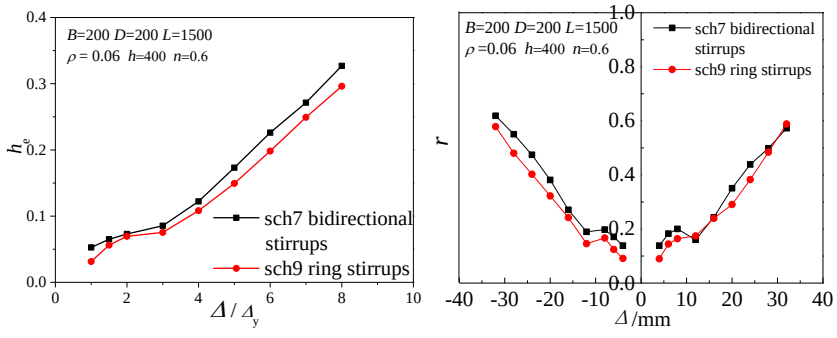

(d) Energy dissipation (e) Residual deformation

Fig.15. Influence of stirrup form on hysteresis behavior

4.6. Effect of loading direction

Fig. 16 and Fig. 17 show the difference of loading direction on the hysteretic behavior of the specimens, when n are 0.2 and 0.7, respectively. It is explained from Fig. 16, Fig. 17 and Table 1 that the hysteresis curve of strong axis loading is plumper than that of weak axis loading. In addition, P, K of each

hysteresis loop, h_e and r of strong axis loading are larger than those of weak axis loading. Compared to specimens rch5, rch6, the DI of rch1, rch3 are decreased from 4.83, 2.48 to 4.54, 2.26, decreased by 6.0%, 8.9%. The difference between DI of them is not significant, indicating that the loading direction has little influence on the ductility of rectangular SCFT specimens.

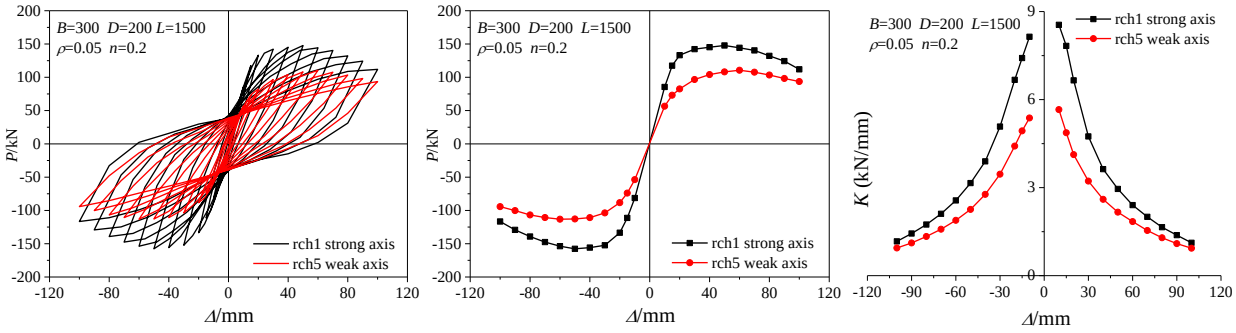

(a) Hysteretic curve (b) Skeleton curve (c) Stiffness degradation

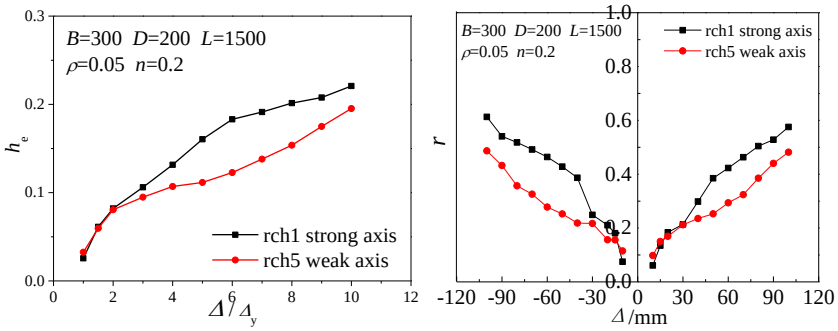

(d) Energy dissipation (e) Residual deformation

Fig.16. Influence of loading direction on hysteresis behavior when *n* is 0.2

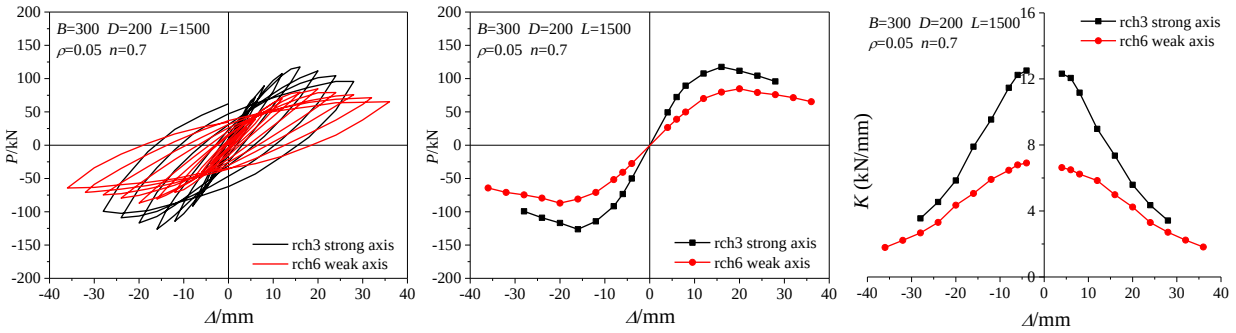

(a) Hysteretic curve (b) Skeleton curve (c) Stiffness degradation

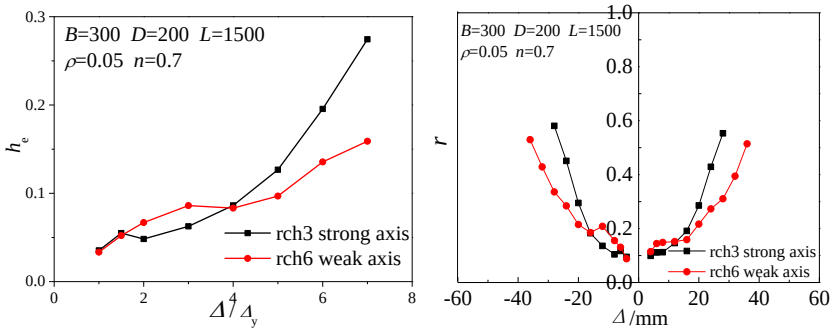

(d) Energy dissipation (e) Residual deformation

Fig.17. Influence of loading direction on hysteresis behavior when *n* is 0.7

4.7. Effect of height-length ratio (*L*/*B*)

Fig. 18 compares the influence of different height-length ratios (*L*/*B*) on the hysteresis curve of specimens. As seen from Fig. 18 and Table 1, the higher the *L*/*B* is, the less the *P* and the K_1 are, the faster the horizontal load decreases, the worse the seismic behavior and the hysteresis loops are slightly pinched. Compared to sch6, the *L*/*B* of sch4 and sch11 are increased from 4.5 to 7.5, 10, increased by 66.7%, 122.0%, respectively. But the *DI* decreases from 4.71 to 4.38, 4.08, decreases by 7.0%, 13.4%, respectively. Similarly, compared to sch7, the *L*/*B* of sch12 is increased from 7.5 to 10, increased by 33.3%, respectively. The *DI* decreases from 2.85 to 2.63, decreases by 7.7%. What's more, compared to rch1, rch2 and rch7, the *L*/*B* of rch8, rch9 and rch6 are increased from 5, 5, 5 to 6.7, 6.7, 7.5, increased by 34.0%, 34.0%, 50% respectively. The *DI* decreases from 4.54, 4.27, 2.75 to 4.12, 3.85, 2.47, decreases by 9.3%, 9.8%, 10.2%. It can be found that when the *L*/*B* increases significantly, the *DI* of the rectangular SCFT decreases very finitely.

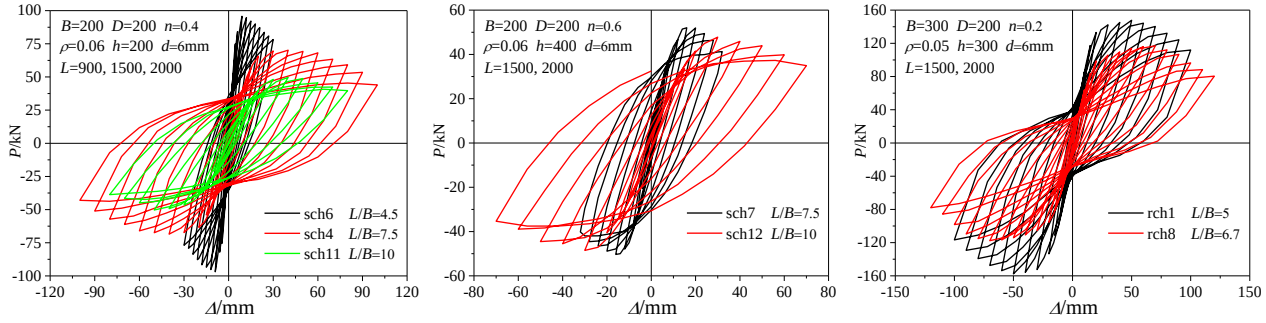

(a) sch6, sch4 and sch11 (b) sch7 and sch12 (c) rch1 and rch8

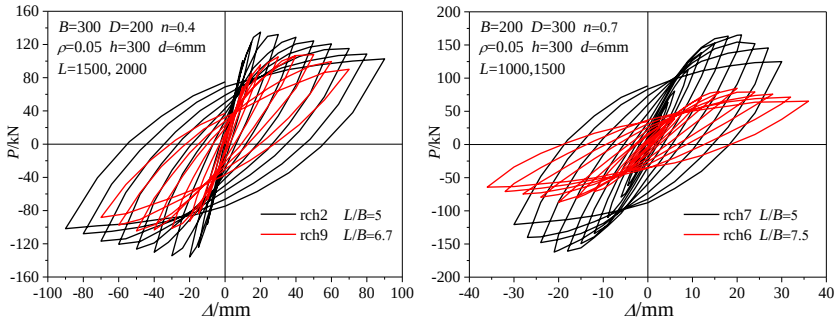

(d) rch2 and rch9 (e) rch7 and rch6

Fig.18. Influence of height-length ratio on hysteresis curve

4.8. Effect of length-width ratio (*B*/*D*)

Fig. 19 and Fig. 20 compare the effect of two length-width ratios *B*/*D*=1 (square SCFT) and *B*/*D*=1.5 (rectangular SCFT) on hysteresis curve and energy dissipation, respectively. It is indicated from Fig. 19, Fig. 20 and Table 1 that when *B*/*D*=1.5, both the *K* and the *P* are larger. But the hysteresis loops demonstrate slightly pinched. On the contrary, when *B*/*D*=1.0, both the *K* and the *P* are smaller. But the hysteresis loops are plumper without pinched. At the same displacement, h_e of square SCFT is greater than that of rectangular SCFT which indicates that the energy dissipation capacity of square SCFT is superior to that of rectangular SCFT. Compared to square SCFT rch3, sch10, sch11 and sch12, the *DI* of rch2, rch8, rch9 and rch10 are decreased from 4.38, 4.62, 4.08 and 3.63 to 4.27, 4.22, 3.85 and 3.39, decreased by 2.5%, 8.7%, 5.6% and 6.6% respectively. It states that the influence of length-width ratio on the *DI* of these rectangular SCFT is tiny.

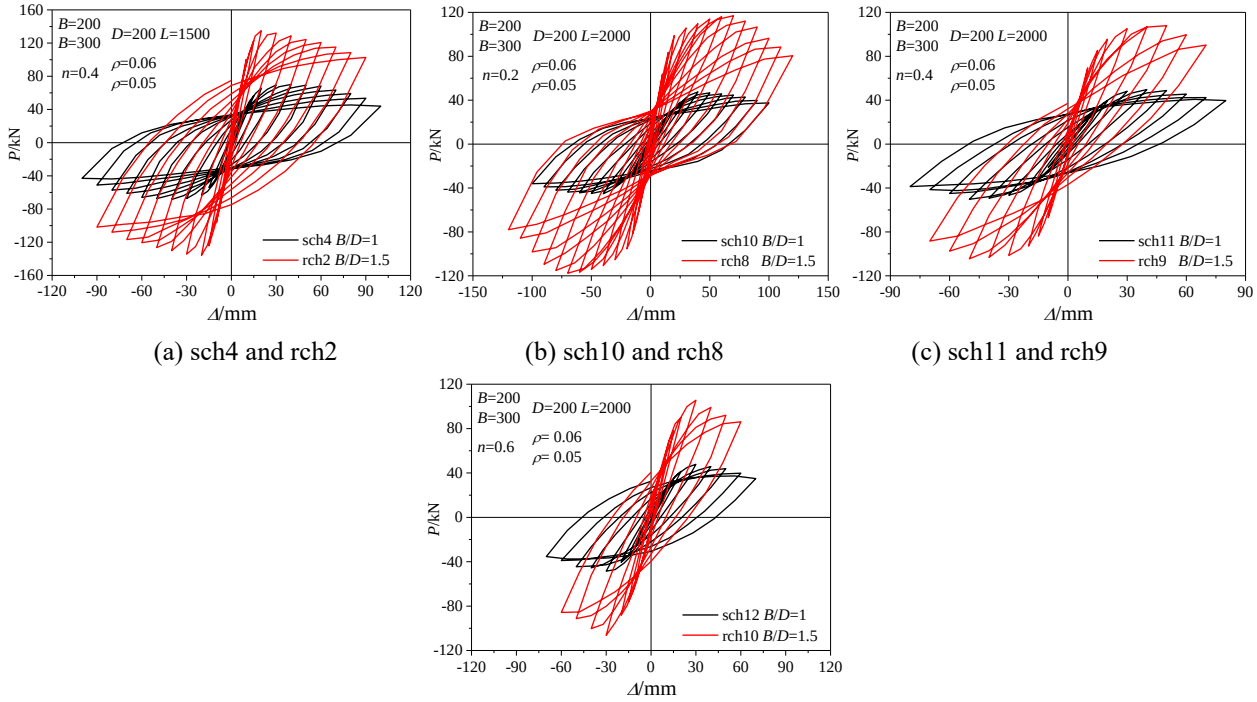

(a) sch4 and rch2 (b) sch10 and rch8 (c) sch11 and rch9

(d) sch12 and rch10

Fig.19. Influence of length-width ratio on hysteresis curve

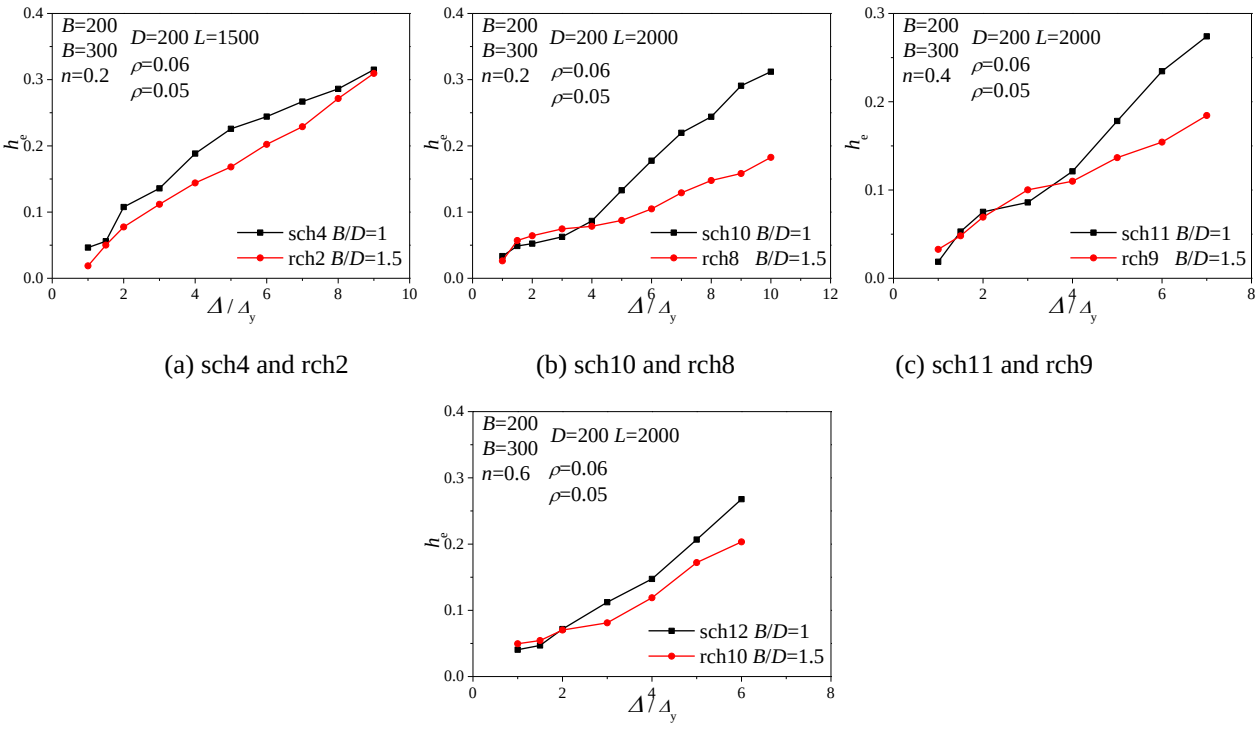

(a) sch4 and rch2 (b) sch10 and rch8 (c) sch11 and rch9

(d) sch12 and rch10

Fig.20. Influence of length-width ratio on equivalent viscous damping index

4.9. Effect of axial compression ratio (*n*)

Fig.s 21, 22, 23, 24 compared the effects of different *n* on the hysteretic curves, stiffness degradation, *DI* and h_e. With the increase of *n*, the initial stiffness of the specimens is generally increased, but descends steeper and the *DI* is obviously reduced. The *DI* of rectangular SCFT with small *n* or medium *n* is generally larger than 3, indicating that the ductility of the specimens is good and can meet the seismic design requirements. Among all specimens, the *DI* of rch3 is the least, which is 2.26 due to its low ρ_{sa} and

high value of n (n=0.7). Based on the "General yield bending moment method", the failure displacement Δ_u of rch3 is 26.0mm. Accordingly, the maximum displacement angle (Δ_u/L) is 1/58, which cannot meet the limit value 1/50 of relevant standards [28, 29]. Therefore it is necessary to increase the ρ_{sa} and conduct the corresponding experimental study. When n increases from 0 to 0.4 or from 0.2 to 0.4, the P of the specimens is generally increased. However, when n is further increased to 0.6 or 0.7, the P is decreased, while the K_1 of the specimen is generally increased. With the increase of the n, the hysteresis loop is plumper and h_e is generally increased, indicating that the energy dissipation capacity is enhanced. For reinforced concrete members in seismic field, the h_e values is approximately 0.1~0.2 [30]. By contrast, the h_e values of the SCFT specimens in this test range from 0.15 to 0.4, which demonstrate that the energy dissipation capacity of SCFT is better than that of reinforced concrete members.

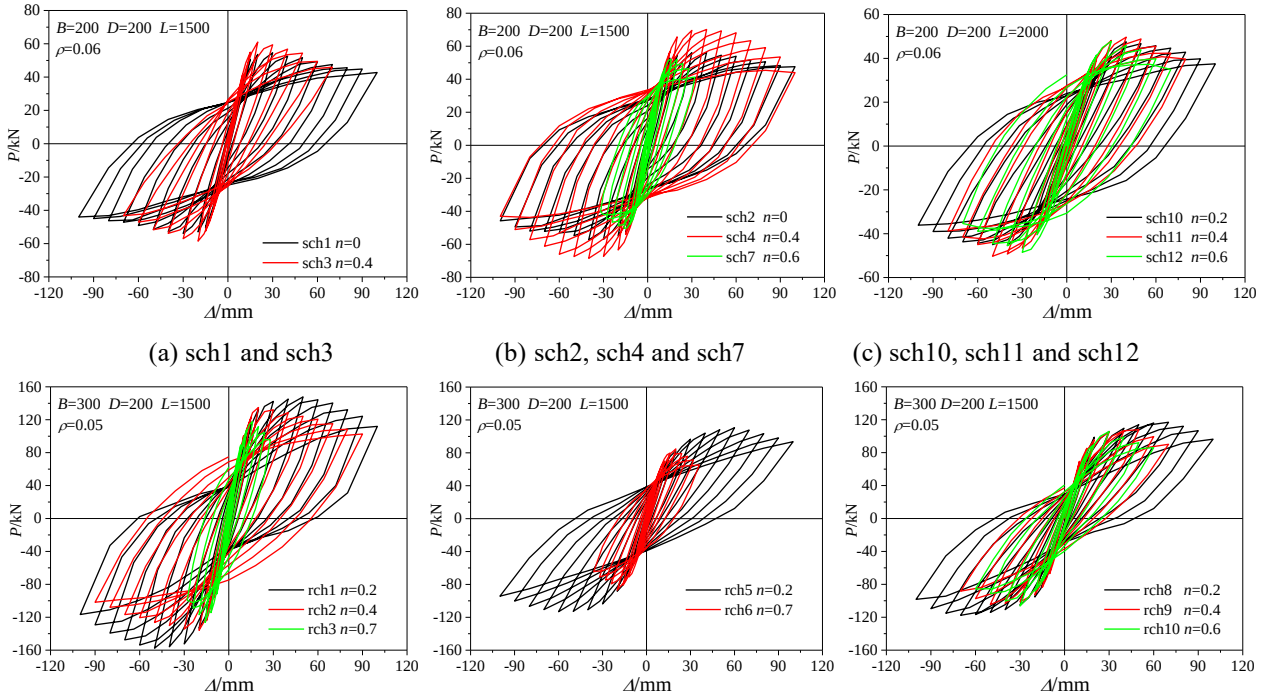

(a) sch1 and sch3 (b) sch2, sch4 and sch7 (c) sch10, sch11 and sch12

(d) rch1, rch2 and rch3 (e) rch5 and rch6 (f) rch8, rch9 and rch10

Fig.21. Influence of *n* on hysteresis curve

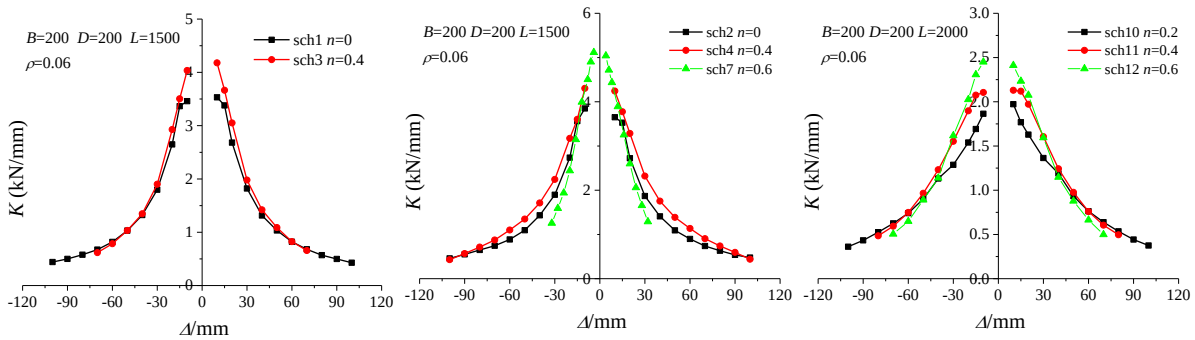

(a) sch1 and sch3 (b) sch2, sch4 and sch7 (c) sch10 and sch1

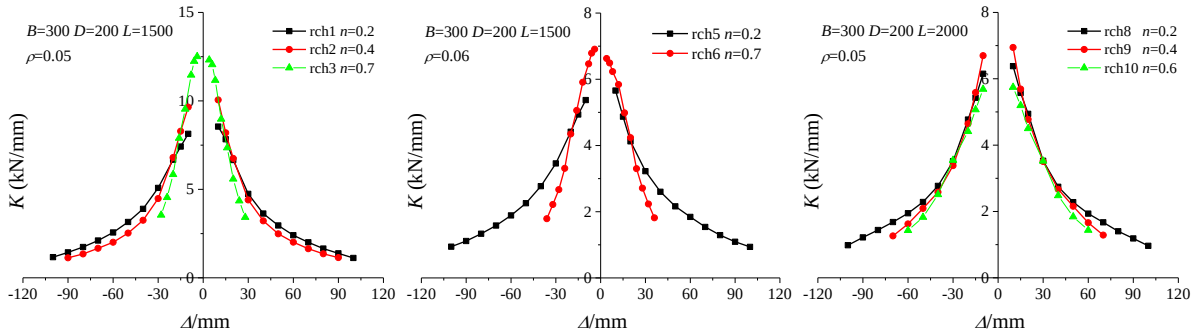

(d) rch1, rch2 and rch3 (e) rch5 and rch6 (f) rch8, rch9 and rch10

Fig.22. Influence of *n* on stiffness degradation

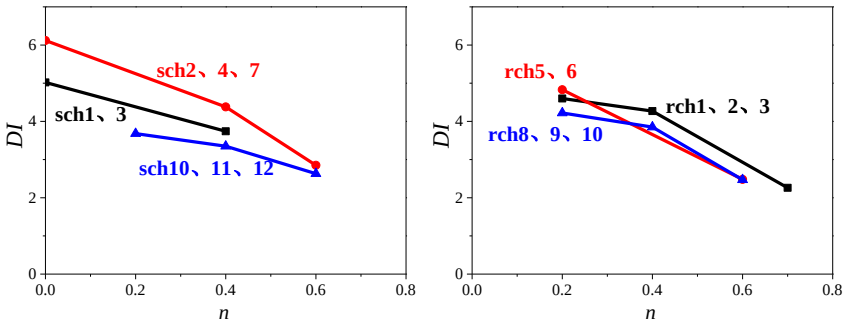

(a) *DI*-*n* of square specimens (b) *DI*-*n* of rectangular specimens

Fig.23. *DI*-*n* relationship curve

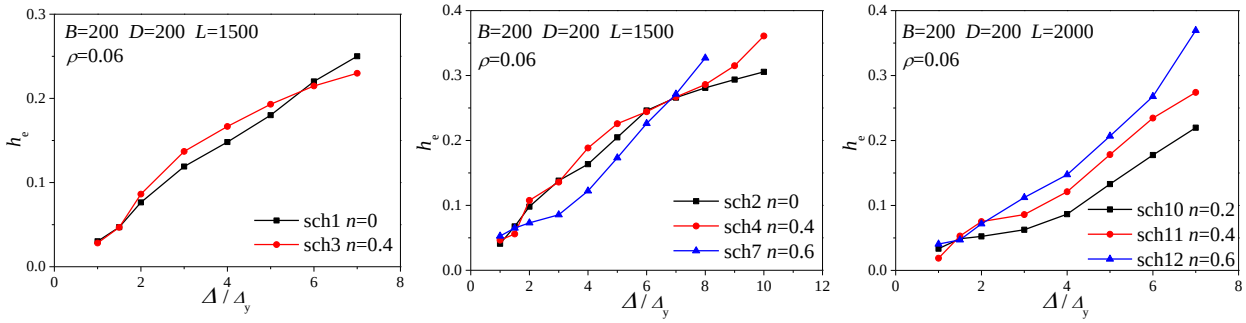

(a) sch1 and sch3 (b) sch2, sch4 and sch7 (c) sch10, sch11 and sch12

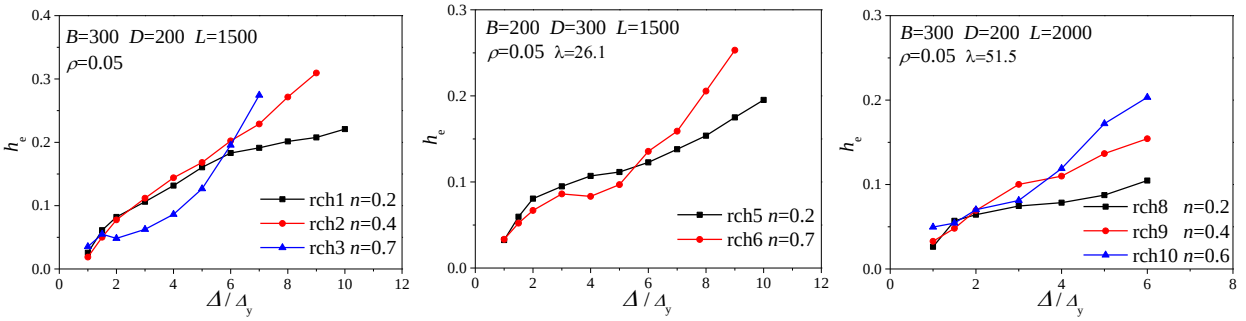

(d) rch1, rch2 and rch3 (e) rch5 and rch6 (f) rch8, rch9 and rch10

Fig.24. Influence of *n* on equivalent viscous damping index

4.10. Effect of sliding support

Fig. 25 compares the effect of sliding support on the hysteresis behavior when *n* is 0.4 and the stirrups range is 200mm (*B*). Because the friction between the jack and the top plate is eliminated due to the sliding support, the skeleton curve of sch3 declines more gently and its stiffness degrade more slowly than sch5.

Also, we can see from Table 1 that the *DI* of sch3 increased from 3.35 to 3.74, increased by 11.6%. However, friction leads the K_1 of sch5 increase from 4.11kN/mm to 4.96kN/mm and the *P* of sch5 increased from 61.02kN to 66.81kN, increased by 20.7% and 9.5%, respectively. In addition, the hysteresis curve of sch5 is plumper and its maximum h_e increased from 0.23 to 0.34, increased by 47.8%.The above results contribute that the impact of friction cannot be ignored in the test , and the sliding support can ensure the experimental data more accurate.

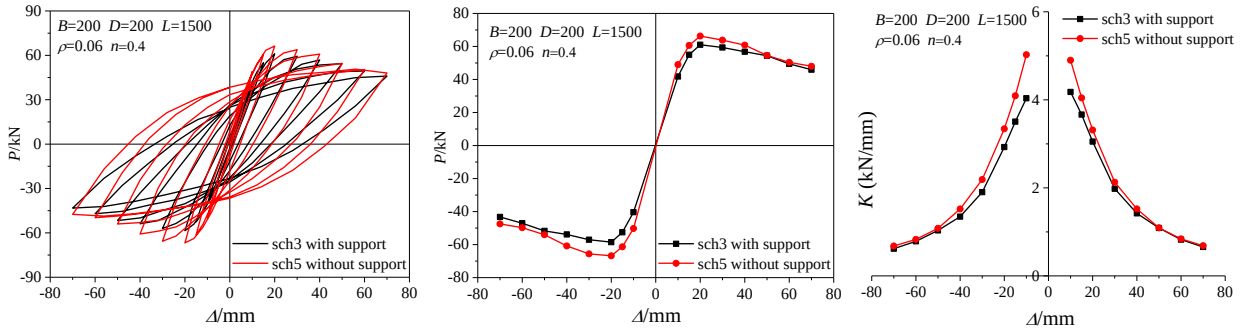

(a) Hysteretic curve (b) Skeleton curve (c) Stiffness degradation

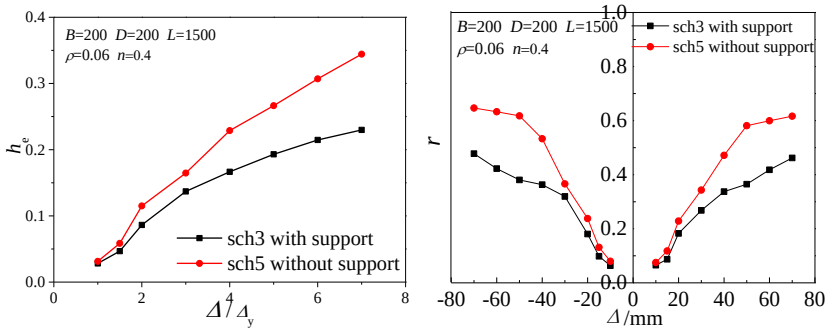

(d) Energy dissipation (e) Residual deformation

Fig.25. Influence of sliding support on hysteresis behavior

5. Conclusions

This paper presents a pseudo-static experimental study on the seismic behavior of stirrup-confined concrete-filled rectangular steel tubular columns. The experimental program consists of 26 specimens with consideration of with or without stirrups, height of terminal stirrup region, equivalent stirrup ratio, loading direction, and axial compression ratio etc. Based on the results of failure mode, strain ratio, ultimate bearing capacity ductility, stiffness degradation, energy dissipation, and residual deformation, the following conclusions can be drawn:

(1) Under axial pressure and horizontal low cyclic load, the specimens are failed mainly by buckling of the steel tubes, crush of the core concrete and fracture of the stirrups. The equivalent viscous damping index of the specimens ranges from 0.15 to 0.4, which demonstrates that they have good seismic energy dissipation capacity.

(2) The maximum strain ratio of typical specimens is more than 0.5, showing that the steel tube exerts a good confinement on the core concrete. The axial pressure can increase the confining effect of steel tube to the core concrete. In addition, the stirrups can directly confine the core concrete, and reduce the maximum strain ratio of the steel tube.

(3) When the axial compression ratio is larger, the bidirectional stirrups can delay local buckling of steel tube, improve the confinement effect on the core concrete effectively, and thus increase the ultimate bearing capacity and ductility index, so as to significantly improve the seismic behavior of the rectangular SCFT columns. At the same axial compression ratio, increasing height of terminal stirrup region or

increasing equivalent stirrup ratio can also effectively improve the seismic behavior of the specimens.

(4) The ultimate bearing capacity of the rectangular SCFT of strong axis loading is distinctly greater than that of weak axis loading, but there is no obvious difference between their ductility. When the height-length ratio and length-width ratio increases, the ductility *DI* decreases very limited.

Acknowledgment

This research work was financially supported by the National Key Research Program of China, Grant No. 2017YFC0703404.

References

[1] X. Chang, C.K. Huang, Y.J. Chen, Mechanical performance of eccentrically loaded pre-stressing concrete filled circular steel tube columns by means of expansive cement, Eng. Struct. 31 (11) (2009) 2588-2597.

[2] X. Chang, L. Fu, H.B. Zhao, Y.C. Song, Behaviors of axially loaded circular concrete-filled steel tube (CFT) stub columns with notch in steel tubes, Thin-Walled Struct. 73 (12) (2013) 273-280.

[3] X. Chang, X.L. Luo, C.X. Zhu, C.A. Tang, Analysis of circular concrete-filled steel tube (CFT) support in high ground stress conditions, Tunn. Undergr. Space Technol. 43 (3) (2014) 41-48.

[4] M.F. Hassanein, O.F. Kharoob, Compressive strength of circular concrete-filled double skin tubular short columns, Thin-Walled Struct. 77 (4) (2014) 165-173.

[5] M.F. Hassanein, O.F. Kharoob, L. Gardner, Behaviour and design of square concrete-filled double skin tubular columns with inner circular tubes, Eng. Struct.100 (10) (2015) 410-424.

[6] Y.S. Huang, Y.L. Long, J. Cai, Ultimate strength of rectangular concrete-filled steel tubular (CFT) stub columns under axial compression, Steel Compos. Struct. 8 (2) (2008) 115-128.

[7] B. Evirgen, A. Tuncan, K. Taskin, Structural behavior of concrete filled steel tubular sections (CFT/CFSt) under axial compression, Thin-Walled Struct. 80 (7) (2014) 46-56.

[8] X.S. Qu, Z.H. Chen. G.J. Sun. Axial behaviour of rectangular concrete-filled cold-formed steel tubular columns with different loading methods, Steel Compos. Struct. 18 (1) (2015) 71-90.

[9] Y.S. Du, Z.H. Chen, M.X. Xiong, Experimental behavior and design method of rectangular concrete-filled tubular columns using Q460 high-strength steel, Constr. Build. Mater. 125 (30) (2016) 856-872.

[10] A.H. Varma, J.M. Ricles, R. Sause, L.W. Lu, Seismic behavior and design of high-strength square concrete-filled steel tube beam columns, J. Struct. Eng. 130 (2) (2004) 169-179.

[11] J.P. Liu, X.H. Zhou, S.M. Zhang, Seismic behaviour of square CFT beam–columns under biaxial bending moment, J. Constr. Steel Res. 64 (12) (2008) 1473–1482.

[12] L.H. Han, Y.F. Yang, Z. Tao, Concrete-filled thin-walled steel SHS and RHS beam-columns subjected to cyclic loading, Thin-Walled Struct. 41 (9) (2003) 801-833.

[13] X.Y. Mao, Y. Xiao, Seismic behavior of confined square CFT columns, Eng. Struct. 28 (10) (2006) 1378-1386.

[14] M.C. Zhu, J.X. Liu, Q.X. Wang, Experimental study of square steel tubes filled with steel-reinforced high-strength concrete. China Civil Eng. J. 44 (7) (2011) 55-63. (in Chinese)

[15] Y.C. Zhang, C. Xu, X.Z. Lu. Experimental study of hysteretic behaviour for concrete-filled square thin-walled steel tubular columns, J. Constr. Steel Res. 63 (3) (2007) 162–175.

[16] Y.T. Wang, J. Cai, Y.L. Long. Hysteretic behavior of square CFT columns with binding bars, J. Constr. Steel Res. 131 (4) (2017) 162–175.

[17] F.X. Ding, D.R. Lu, Y. Bai, Q.S. Zhou, N. M, Z.W. Yu, G.S. Jiang, Comparative study of square stirrup-confined concrete-filled steel tubular stub columns under axial loading. Thin-Walled Struct. 98

(1) (2016) 443-453.
[18] F.X. Ding, L. Fu, X.M. Liu, J. Liu, Mechanical performances of track-shaped rebar stiffened concrete-filled steel tubular (SCFRT) stub columns under axial compression. Thin-Walled Struct. 99 (2) (2016) 168-181.
[19] F.X. Ding, X.Y. Ying, L.C. Zhou, Z.W. Yu, Unified calculation method and its application in determining the uniaxial mechanical properties of concrete. Front. Archit. Civ. Eng. China 5(3) (2011) 381-393.
[20] GB 50017-2003. Code for design of steel structures. China Planning Press, Beijing, 2003.
[21] GB/T50081-2002. Standard for method of mechanical properties on ordinary concrete. China Building Industry Press, Beijing, 2002.
[22] GB/T228-2002. Metallic materials-tensile testing at ambient temperatures. Standards Press of China, Beijing, 2002.
[23] JGJ/T 101-2015. Specification for seismic test of buildings. Building Industry Press, Beijing, 2015.
[24] Z.W. Yu, F.X. Ding, C.S. Cai, Experimental behavior of circular concrete-filled steel tube stub columns, J. Constr. Steel. Res. 63 (2) (2007) 165–174.
[25] J.Y. Xue, H. Ma, Y. Liu, Experimental study on seismic performance of steel reinforced recycled concrete columns under low-cyclic reversed loading, China Civil Eng. J. 47(1) (2014) 36-46.
[26] J.G. Nie, J.S. Fan, X.G. Liu, Y, Huang, Comparative study on steel plate shear walls used in a high-rise building, J. Struct. Eng. 139 (1) (2013) 85-97.
[27] J.G. Nie, K. Qing, R. Liu, Experimental study on seismic behavior of connections composed of concrete-filled square steel tubular columns and steel-concrete composite beams with interior diaphragms, China Build. Struct. J. 27 (4) (2006) 1-9.
[28] GB50936-2014. Technical code of concrete filled steel tubular structures.: Building Industry Press, Beijing, 2014.
[29] CECS159:2004. Technical specification for structures with concrete-filled rectangular steel tube members. China Planning Press, Beijing, 2004.
[30] M. Eduardo, R.G. Jorge, Evaluation of approximate methods to estimate maximum inelastic displacement demands. Earthquake Eng. Struct. Dyn. 31 (3) (2002) 539-560.